A prognostic model for human papillomavirus-negative head and neck squamous cell carcinoma based on a novel ferroptosis-related gene signature: Development, validation and elucidation of its relationship with the immune microenvironment

JIAO LI[1,2], NURHAYU AB RAHMAN[2], SUHARNI MOHAMAD[3] and GUANG YANG[4]

[1]Department of Pathology, Heping Hospital Affiliated to Changzhi Medical College, Changzhi, Shanxi 046000, P.R. China; [2]Oral Medicine and Oral Pathology Unit, School of Dental Sciences, Universiti Sains Malaysia Health Campus, 16150 Kota Bharu, Kelantan, Malaysia; [3]Basic Science Unit, School of Dental Sciences, Universiti Sains Malaysia Health Campus, 16150 Kota Bharu, Kelantan, Malaysia; [4]Department of General Surgery, Ruijin Hospital, Shanghai Jiao Tong University School of Medicine, Shanghai 200000, P.R. China

Received May 23, 2025; Accepted October 23, 2025

DOI: 10.3892/ol.2025.15425

Abstract. Head and neck squamous cell carcinoma (HNSCC) can be categorized as human papillomavirus (HPV)-positive or -negative. The present study explored the potential prognostic value of ferroptosis-related genes (FRGs) and their impact on the tumor immune microenvironment in HPV-negative HNSCC compared with HPV-positive HNSCC, based on data from The Cancer Genome Atlas online database. The bioinformatics analysis results were then verified through cell culture and histological analyses. The prognostic model was developed by evaluating the correlations between prognostic value and the expression of FRGs in HPV-negative HNSCC. This was based on differential analysis of data from The Cancer Genome Atlas between the HPV-negative and -positive patient subgroups. The relationships of the identified hub FRGs with immune cell infiltration were determined by CIBERSORT R scripts for the HPV-negative subgroup. Tribbles pseudokinase 3 (TRIB3) expression in both HPV-negative and -positive HNSCC cells was verified by reverse transcription-quantitative polymerase chain reaction, western blotting and immunohistochemistry. The role of TRIB3 in mediating ferroptosis in both HPV-positive and -negative cells was validated by transmission electron microscopy and intracellular Fe^{2+}, reactive oxygen species (ROS), glutathione (GSH) and malondialdehyde (MDA) assessments. As a result, it was verified that the prognostic model for HPV-negative patients had a good performance. TRIB3 expression was higher in HPV-negative samples than in HPV-positive samples. Additionally, following cell transfection, *TRIB3* knockdown increased intracellular Fe^{2+}, MDA and ROS levels, decreased GSH levels and diminished or eliminated mitochondrial ridges in HPV-negative cells. By contrast, *TRIB3* overexpression decreased intracellular Fe^{2+}, MDA and ROS, while increasing GSH in HPV-positive cells. In conclusion, the constructed model may indicate the prognosis of patients with HPV-negative HNSCC. Moreover, *TRIB3*, via its involvement in ferroptosis, may serve as a potential therapeutic target for both HPV-positive and HPV-negative HNSCC. Thus, the present study has provided a starting point for further investigation into the therapeutic potential of targeting *TRIB3*.

Correspondence to: Dr Guang Yang, Department of General Surgery, Ruijin Hospital, Shanghai Jiao Tong University School of Medicine, 197 Ruijin Er Road, Huangpu, Shanghai 200000, P.R. China
E-mail: yg13162@rjh.com.cn

Key words: head and neck squamous cell carcinoma, human papillomavirus-negative, ferroptosis, The Cancer Genome Atlas, prognostic model, immune infiltration

Introduction

In 2020, the global number of deaths from head and neck cancer (HNC), which includes cancer of different regions, such as the salivary glands, lips and oral cavity, larynx, hypopharynx, nasopharynx and oropharynx, reached 440,000 (1,2). Head and neck squamous cell carcinoma (HNSCC), the predominant histological type of HNC, originates from the mucosal epithelia of the buccal cavity, pharynx and larynx, and accounts for >90% of all cases of HNC (3,4). HNSCC can be categorized as human papillomavirus (HPV)-positive or HPV-negative. The biological characteristics of HNSCC notably differ between patients owing to the impact of HPV (5). In a previous study, patients with oropharyngeal squamous cell carcinoma who tested positive for HPV had a 5-year overall survival (OS) rate of 81.1%, while those with HPV-negative malignancies had a survival rate of 39.7% (6).

The treatment of HNSCC is complicated by the resistance of cancerous cells to chemotherapy. Resistance to chemotherapy is primarily attributed to the inefficacy of most chemotherapy medications for inducing cell death in resistant tumor cells. This inefficacy is influenced by several factors,

including DNA damage repair, cell cycle regulation, immune invasion, tumor progression, tumor recurrence induced by the impact of severe acute respiratory syndrome coronavirus 2-mediated triggering of various intracellular signaling axes, the presence of tumor-associated stem cells, autophagy, epithelial-to-mesenchymal transition and the effects of efflux pumps and metabolic rewiring (7-13). Therefore, it is essential to develop new strategies to predict clinical outcomes, and to design personalized treatment strategies for patients with HNSCC, especially HPV-negative HNSCC.

In recent decades, several new non-apoptotic methods of controlled cell death have been identified, such as pyroptosis, ferroptosis, necroptosis, alkaliptosis and cuproptosis. These are potentially useful tools in the context of cancer therapy (14-18). Each of these processes has distinct biological mechanisms and pathological characteristics. Ferroptosis, which was first proposed by Dixon *et al* (19), is an iron-dependent form of cell death that is characterized by the intracellular generation of lipid reactive oxygen species (ROS). Previous studies have shown that there are marked differences between ferroptosis and other forms of cell death, such as apoptosis, necrosis and autophagy, in terms of morphology (for example, shrunken mitochondria with increased membrane density), biochemistry (iron-mediated lethal lipid ROS accumulation and no ATP depletion), and genetics (governed by unique genes such as ribosomal protein L8 and iron responsive element binding protein 2, independent of Bax/Bak) (19,20).

Ferroptotic agents could provide an effective approach to address the inefficacy of apoptosis-inducing chemotherapeutics, since ferroptosis differs completely from apoptosis in terms of its mechanism for inducing cell death (19). The importance of ferroptosis in the development and advancement of diverse diseases has been recognized such as in malignancies, neurodegenerative conditions and ischemia-reperfusion damage (21). There has been an increased focus on the potential applications of ferroptosis in cancer therapy for improving prognosis and overcoming drug resistance (18,22,23). In HNSCC cells, ferroptosis can decrease or reverse tumor cell resistance to chemotherapy (24-26). The immune system controls the therapeutic response of cancer and impedes progression, infiltration and metastasis. Immune surveillance functions as a mechanism to detect, regulate and eradicate malignant cells (27-29). *In vivo*, treatment with programmed death-ligand 1 blockers and glutathione (GSH) elimination can induce ferroptosis in tumor cells and activate the antitumor activity of T lymphocytes (30). A previous study demonstrated that immunological B cells triggered an immune response that suppressed tumor growth and was associated with ferroptosis by increasing the dendritic cell count in patients with oral cancer (31). Thus, stimulating ferroptosis in tumor cells could be an effective approach to tumor treatment.

To date, most studies have primarily focused on the differences in ferroptosis between healthy individuals and patients with HNSCC (31,32). However, the potential differences between HPV-positive and HPV-negative HNSCC in terms of ferroptosis-related genes (FRGs) have received little attention. Furthermore, previous studies (31,32) have merely focused on verifying the molecular characteristics of genes from the incorporated prognostic models, without an in-depth analysis to determine their regulatory role in the ferroptosis of HNSCC cells. Therefore, the present study aimed to identify the FRGs with significant involvement in HPV-negative HNSCC (which has a particularly poor prognosis), to develop a predictive model using the FRG signatures of HPV-negative HNSCC and to explore the associations of these FRGs with the immune microenvironment (IME). The present study also aimed to verify the specific functions of the most promising FRGs based on the prognostic model. The successful identification of such genes is expected to assist prognosis predictions and enable targeted treatment, thereby enhancing the clinical outcomes of patients with HPV-negative HNSCC.

Materials and methods

Data sources. The source of the clinical data was a publication by Hoadley *et al* (33). The HNSCC datasets containing the transcript data were attained from The Cancer Genome Atlas (TCGA) database (https://portal.gdc.cancer.gov/) on February 17, 2024. There were 487 HNSCC samples, including 415 HPV-negative and 72 HPV-positive samples, included in the TCGA-HNSCC dataset. Gene Set Enrichment Analysis (GSEA) and hallmark datasets from the Molecular Signatures Database (https://www.gsea-msigdb.org/gsea/msigdb/) were utilized to identify relevant genes and pathways. The database used for researching ferroptosis and FRGs is available at http://www.zhounan.org/ferrdb. Genes associated with ferroptosis, including driver, suppressor and marker genes, were downloaded to avoid omission. Additionally, GSE83519 (34) data were downloaded from https://www.ncbi.nlm.nih.gov/geo/.

Identification of FRGs. First, the FRG expression matrix was obtained using R software (RStudio 2022.07.2). The 'limma' package of R (version 3.52.4) was used to identify differences in the expression of FRGs between the HPV-negative and HPV-positive samples from the TCGA-HNSCC group.

Consensus clustering. Consensus clustering was conducted using the *k*-means method in the 'ConsensusClusterPlus' package of R (version 1.60.0) to identify distinct patterns related to the FRGs. The clustering accuracy was confirmed using Uniform Manifold Approximation and Projection (UMAP) in the 'ggplot2' package of R (version 3.3.6).

Identification and validation of prognostic signatures based on the FRGs. Least Absolute Shrinkage and Selection Operator (LASSO) regression analysis was conducted using the 'glmnet' package of R (version 4.1.4) to identify genes associated with survival. Next, 10-fold cross-validation was used to determine the penalty regularization value (λ). The key genes and their accompanying coefficients were then determined using multivariate Cox regression analysis. In total, 10 FRGs were selected as risk signatures based on the optimal λ values and their corresponding coefficients. The following formula was used to determine the risk score for each patient using the new FRG signature: $Riskscore=\Sigma exp_i \times \beta_i$ where β and exp represent the coefficient and the expression level of the corresponding gene in the multivariate Cox regression model, respectively.

For external validation, it was found that most Gene Expression Omnibus datasets either lacked explicit HPV status annotations or did not include paired prognostic information, making them unsuitable for validating the constructed HPV-subtype-specific prognostic model. Thereafter, comprehensive internal validation on the TCGA-HNSC cohort was performed by randomly partitioning the data into three independent subsets: Training, testing and combined cohorts. The predictive performance of the model was assessed through time-dependent receiver operating characteristic (ROC) curve analyses, and the area under the curve (AUC) was defined as the area enclosed by the ROC curve and the coordinate axes. Additionally, Kaplan-Meier survival analysis curves were generated. The ROC curve and Kaplan-Meier survival analyses were performed using R software (RStudio 2022.07.2) through 'timeROC' (version 0.4) and 'survival' (version 3.4.0) R packages, respectively.

Construction and examination of the predictive nomogram. The nomogram was generated based on risk scores and clinicopathological features. Internal validation of accuracy was performed using a calibration curve. The predictive performance of the nomogram was evaluated using the time C-index. To assess the net clinical benefit, decision curve analysis (DCA) was performed (35).

Associations between immune cell infiltration and risk score. The quantification of infiltrated immune cell percentages was conducted using both the CIBERSORT R script and the single sample GSEA R script following previously reported methods (36). The distributions of immune cell types among the groups were compared using CIBERSORT R. Each sample showed an aggregated inferred score of 1 for the immune cell types. Score 1 indicates that the sum of the relative proportions of all immune cell types inferred in the sample equals 1, which is equivalent to 100%. Furthermore, Spearman's rank correlation analysis was used to ascertain the associations between the infiltration of immune cells and risk scores.

Drug sensitivity analysis. For determining how effectively a patient responded to treatment, drug sensitivity, also known as the half maximum inhibitory concentration (IC_{50}), was an essential statistic. Through the Genomics of Drug Sensitivity in Cancer database, the IC_{50} measurements were utilized to demonstrate the sensitivity of each drug to each sample. The R package known as 'oncoPredict' (37) was utilized to make predictions regarding the response of anticancer treatments for each HNSCC sample that was differentiated into the low-risk and high-risk groups. All statistical analyses are represented using the 'ggplot2' R package (version 3.3.6).

Cell culture. The HNSCC CAL27 (HPV-negative) and UPCI-SCC-090 (HPV-positive) cell lines were obtained from Procell Life Science & Technology Co. Ltd., and Zhejiang Meisen Cell Technology Co., Ltd., respectively. CAL27 cells were cultured in high-glucose Dulbecco's modified Eagle's medium (DMEM; Procell Life Science & Technology Co. Ltd.) with 10% fetal bovine serum (FBS; Procell Life Science & Technology Co. Ltd.), while UPCI-SCC-090 cells were cultured in DMEM/F-12 (Zhejiang Meisen Cell Technology Co., Ltd.) with 10% FBS. The cells were maintained at 37˚C in a humidified atmosphere containing 5% CO_2.

Reverse transcription-quantitative polymerase chain reaction (RT-qPCR). Total RNA was isolated from CAL27 and UPCI-SCC-090 cells using the Total RNA extraction kit (cat. no. R1200; Beijing Solarbio Science & Technology Co., Ltd.) and reverse transcribed into complementary DNA using the reverse transcription kit (cat. no. 11141ES60; Shanghai Yeasen Biotechnology Co., Ltd.) following the manufacturer's instructions. qPCR was performed using Realtime PCR fluorescence quantitative kit (Hieff® qPCR SYBR Green Master Mix; cat. no. 11201ES08; Shanghai Yeasen Biotechnology Co., Ltd.) and a Real-time Fluorescence Quantitative PCR Instrument (Suzhou Molarray Co., Ltd.) and the following thermocycler conditions: 95˚C for 5 min, followed by 40 cycles at 95˚C for 10 sec, 60˚C for 20 sec and 72˚C for 20 sec. The primer sequences are shown in Table SI. The $2^{-\Delta\Delta Cq}$ method was used to calculate relative gene expression (38). GAPDH was used as an internal control to normalize the expression levels of target genes, correcting for variations in RNA input and RT efficiency.

Cell transfection of Tribbles pseudokinase 3 (TRIB3) small interfering RNA (siRNA). CAL27 cells were seeded into 6-well plates (cat. no. F603201-9001; Sangon Biotech Co., Ltd.) at a density of $1.5x10^5$ cells/ml, with 2 ml in each well, 24 h before transfection. The siRNA was purchased from OBiO Technology (Shanghai) Corp., Ltd. and Lipofectamine™ 3000 (cat. no. L3000008; Thermo Fisher Scientific, Inc.) was used for transfection. The final concentration of the siRNA knockdown reagent (siTRIB3) and siRNA negative control reagent was 20 pmol/μl, and the experimental volume used for each was 5 μl. The cells were divided into the blank control, negative control and knockdown groups. The blank control group was cells + complete medium, the negative control group was cells + complete medium + transfection reagent + negative control siRNA and the knockdown group was cells + complete medium + transfection reagent + target siRNA. Next, the cells were placed into a 5% CO_2 incubator at 37˚C for further culture. The three TRIB3 siRNAs were transfected separately and the siRNA resulting in the most significant knockdown was selected for subsequent experiments. After culturing for 48 h, RT-qPCR was performed to examine the transfection efficiency and the most efficient siRNA was chosen for the next experiment. The siRNA sequences are displayed in Table SII.

Cell transfection for TRIB3 overexpression. UPCI-SCC-090 cells were digested and seeded into a 6-well plate 24 h prior to transfection at a density of $2x10^5$ cells/ml, with 2 ml in each well. The overexpression plasmid [pcDNA3.1(+)-EGFP] was purchased from SYNBIO Technology (Suzhou) Co., Ltd. (Suzhou Hongxun Biotechnology Co., Ltd.). Lipofectamine™ 3000 (cat. no. L3000008; Thermo Fisher Scientific, Inc.) was used to transfect the cells. The final concentration of the overexpression plasmid and empty plasmid was 1 μg/μl, and the experimental volume used for each was 2 μl. The cells were divided into the blank control, negative control and overexpression groups. The blank control group was cells + complete medium, the negative control group was cells + complete

medium + transfection reagent + empty vector plasmid, and the overexpression group was cells + complete medium + transfection reagent + overexpression plasmid. Next, the cells were incubated at 37˚C in a 5% CO_2 incubator. After 5 h, the medium was replaced with 10% FBS-DMEM, and the cells were cultured for another 48 h before subsequent experiments. The transfection efficiency was verified by RT-qPCR.

Western blotting. Total protein was extracted from the HNSCC cells. For protein extraction, RIPA lysis buffer (cat. no. P0013B; Beyotime Biotechnology) was combined with a protease/phosphatase inhibitor (cat. no. P1045; Beyotime Biotechnology) cocktail at a 1:100 ratio, and the mixture was used immediately. Next, for the quantification of protein concentration, a BCA protein assay kit (cat. no. PC0020; Beijing Solarbio Science & Technology Co., Ltd.) was employed, following the manufacturer's recommended protocol. For electrophoresis, the processed samples were loaded onto the gel with a total mass of 20 μg protein per well. Following separation using 8% sodium dodecyl sulfate-polyacrylamide gel electrophoresis, the extracted proteins were transferred onto polyvinylidene fluoride membranes (cat. no. IPVH00010; MilliporeSigma). Subsequently, the membranes were blocked using 5% non-fat milk for 3 h on a shaker at room temperature and incubated overnight at 4˚C with primary antibodies targeting GAPDH (cat. no. 10494-1-AP; 1:5,000; Proteintech Group Inc.), TRIB3 (cat. no. DF7844; 1:1,000; Affinity Biosciences, Ltd.) and acyl-CoA synthetase long chain family member 1 (ACSL1; cat. no. GTX112430; 1:1,000; GeneTex, Inc.). The secondary antibody was a HRP-conjugated goat anti-rabbit IgG antibody (cat. no. bs-0295G-HRP; 1:5,000; BIOSS), which was incubated with the membrane on a horizontal shaker at room temperature for 1.5 h. Images were acquired with the Automated Chemiluminescent Image Analysis System (Tanon 5200; Tanon Science & Technology Co., Ltd.) following ECL (cat. no. P0018S-2; Beyotime Biotechnology) substrate incubation. Lastly, the intensity of the protein bands was semi-quantified using ImageJ software (version 1.53; National Institutes of Health).

Quantification of ROS. ROS were quantified using the ROS fluorometric assay kit (cat. no. E-BC-K138-F, Wuhan Elabscience Biotechnology Co., Ltd.) according to the manufacturer's guidelines. CAL27 cells (1x10^6 cells/well) were cultured in 6-well plates. Cultured or transfected cells were treated in the dark with the ROS solution for 20 min at 37˚C, then the fluorescence intensity was evaluated by an inverted fluorescence microscope [XD-RFL; Sunny Optical Technology (Group) Co., Ltd.].

Measurement of intracellular Fe^{2+} content. The intracellular Fe^{2+} concentration was quantified using Cell Ferrous Iron Colorimetric assay reagent (cat. no. E-BC-K881-M; Wuhan Elabscience Biotechnology Co., Ltd.). Briefly, the cultured or transfected cells (1x10^6) were mixed with 0.2 ml reagent 1 and incubated in an ice bath for 10 min to facilitate lysis, followed by centrifugation at 15,000 x g for 10 min at room temperature. For further analysis, the absorbance of the supernatants at 593 nm was measured using a microplate reader (Synergy H4; BioTek; Agilent Technologies, Inc.).

Measurement of cellular GSH. The GSH concentration in CAL27 cells was measured using the Reduced GSH Colorimetric Assay Kit (cat. no. E-BC-K030-M; Wuhan Elabscience Biotechnology Co., Ltd.) following the manufacturer's protocol. The absorbance at 405 nm was measured using a microplate reader (Synergy H4; BioTek; Agilent Technologies, Inc.).

Measurement of cellular malondialdehyde (MDA). Cellular MDA was quantified using the Malondialdehyde Colorimetric Assay Kit (cat. no. E-BC-K028-M; Wuhan Elabscience Biotechnology Co., Ltd.) following the manufacturer's instructions. Transfected cells were harvested using an extraction solution. The test samples, blank tubes and standard tubes were incubated at 100˚C for 40 min and then cooled to room temperature in a water bath. The resulting samples were centrifuged in Eppendorf (EP) tubes at 1,078 x g for 10 min at room temperature and 0.25 ml supernatant was transferred to the enzyme-labeled plate. The absorbance of each well was measured at 532 nm using a microplate reader (Synergy H4; BioTek; Agilent Technologies, Inc.).

Flow cytometry. CAL27 cells (1x10^6) were cultured in 6-well plates. After transfection with siTRIB3, the cells were incubated for 24 h before being treated with propidium iodide (Beijing Solarbio Science & Technology Co., Ltd.) for 30 min at 37˚C. Subsequently, the cell cycle distribution was analyzed by flow cytometry (NL-CLC3000; Cytek Biosciences, Inc.) and FlowJo software (10.8.1), with an excitation wavelength of 488 nm.

Transmission electron microscopy. CAL27 cells (both the control group and those transfected with siTRIB3 together with the culture medium) were subjected to centrifugation at 42-107 x g for 5 min at room temperature, followed by careful removal of the resulting supernatant with 1 ml remaining. The CAL27 cell pellet was gently resuspended in the remaining media and transferred to a 1.5-ml EP tube. After allowing the mixture to settle for 1 h, the supernatant was meticulously extracted and 1 ml pre-chilled 2.5% glutaraldehyde was gradually added to the tube along the periphery for fixation. The tube was then placed in a refrigerator at 4˚C for at least 2 h. The cells were subsequently fixed in 1% osmic acid at 4˚C for 2 h. Following fixation, the cells were detached from the plastic surface and dehydrated using ethanol and acetone, respectively. The specimens were embedded in EPON812 embedding solution (SPI-Pon 812 Kit; cat. no. 02663-AB; SPI Supplies; Structure Probe, Inc.) for 2-3 h at 37˚C and sectioned to 70 nm. Thereafter, double staining was carried out: First with 2% uranyl acetate (staining time: 15-20 min at room temperature) and then with lead citrate (staining time: 10-15 min in a CO_2-free environment to avoid precipitation), ensuring sufficient contrast for ultrastructural observation. The sections were then analyzed using an HT7800 (80 kV) transmission electron microscope (Hitachi, Ltd.).

Immunohistochemistry (IHC). Samples from patients with primary HNSCC (with or without comorbidities) who had undergone surgery at the Department of Pathology, Heping Hospital Affiliated to Changzhi Medical College (Changzhi, China) from January 1, 2018 to December 31, 2022 were

included. The patient samples for IHC were used retrospectively. All patients were aged >18 years and had not undergone any other prior treatment (including radiation and chemotherapy). Patients with a history of prior treatments (radiotherapy or chemotherapy) or those with recurrent HNSCC were excluded from the study. In accordance with the predefined inclusion and exclusion criteria, a total of 179 eligible cases were eventually enrolled. Among these patients, the age range was 38 to 87 years, with a mean age of 63.2 years. Regarding sex distribution, 121 patients were men (accounting for 67.6% of the total) and 58 were women (representing 32.4%).

For paraffin-embedded slides (0.4 μm), first the sections were baked in a 60-65˚C preheated oven for 15-20 min to melt the surface paraffin. Then, the sections were sequentially immersed in xylene to completely remove residual paraffin, followed by gradual rehydration via gradient ethanol solutions (from high to low concentration) and finally transitioned to an aqueous environment. After antigen retrieval of paraffin sections (EDTA buffer, 95-100˚C, 20 min) and subsequent cooling to room temperature followed by 2-3 washes with PBS (3-5 min each), permeabilization was performed by immersing the sections in a paraffin section-compatible permeabilization reagent (0.3% Triton X-100 in PBS) for 10-15 min. Next, the sections were blocked with 10% bovine serum albumin (cat. no. C0221; Beijing Solarbio Science & Technology Co., Ltd.) at room temperature for 30 min and then incubated with primary antibodies against TRIB3 (cat. no. bs-7538R; 1:300; BIOSS) and p16 (cat. no. HA721415; 1:200; HUABIO) at 4˚C overnight. Next, the samples were incubated with goat anti-rabbit IgG/biotin secondary antibody (cat. no. SHB134; 1:200; Beijing Solarbio Science & Technology Co., Ltd.) for 2 h at 37˚C. Hematoxylin was used to counterstain the nucleus (1 min, room temperature). Finally, the sections were incubated with 0.05-0.1% 3,3'-diaminobenzidine solution (containing 0.01% H_2O_2, dissolved in Tris-HCl buffer) at room temperature for 3-10 min to allow brown precipitates to form at the target antigen-binding sites, followed by terminating the staining reaction with distilled water. Then, the sections were scanned using a panoramic slice scanner. The present study was approved by the Human Ethical Committee of Heping Hospital Affiliated to Changzhi Medical College [Changzhi, China; approval no. 2023(027)]. The requirement for informed consent was waived by the committee as the risks involved in the study were very low and did not cause significant harm to the participants.

Statistical analysis. Statistical analysis was performed using GraphPad Prism (version 10.0.3; Dotmatics) and R (version 4.2.1). The results are presented as the mean ± standard deviation. Two-group comparisons were performed using the unpaired t-test, while multiple-group comparisons were performed using one-way ANOVA and Tukey's HSD post hoc test. $P<0.05$ was considered to indicate a statistically significant difference.

Results

Identification of FRGs associated with prognosis. In total, 845 FRGs were identified in the ferroptosis database. A comparison between HPV-negative and HPV-positive samples identified 299 differentially expressed FRGs from TCGA-HNSC. When HPV-negative was compared with HPV-positive samples, 208 genes were downregulated, and 91 genes were upregulated in the HPV-negative samples (Table SIII). Univariate Cox regression analysis indicated that 25 of the 300 FRGs had a significant association with survival, as depicted in the forest plot ($P<0.05$; Fig. 1A). *TRIB3* was significantly elevated in HNSCC samples according to the results of TCGA-HNSCC (Fig. S1) and GSE83519 (Fig. S2) analyses. *TRIB3* was also more upregulated in HPV-negative samples than in HPV-positive samples (Table SIII and Fig. S3), suggesting that it may be particularly important in HPV-negative HNSCC. Western blotting (Fig. 1B) and RT-qPCR (Fig. 1C) confirmed that the difference in TRIB3 expression between HNSCC CAL27 (HPV negative) and UPCI-SCC-090 (HPV positive) cells aligned with the results of the bioinformatics analysis. Additionally, ACSL1 expression was also upregulated in HPV-negative cells (Fig. S4). *TRIB3* was associated with the prognostic outcome of patients with HPV-negative HNSCC, but not with that of patients with HPV-positive HNSCC (Fig. 1D and E). The immunohistochemistry results from paraffin-embedded slides of TRIB3 were consistent with those of western blotting and RT-qPCR from cell culture experiments (Fig. 1F).

Consensus clustering of the 25 FRGs in HPV-negative HNSCC. To understand the significance of the FRGs in HPV-negative HNSCC, consensus clustering on the 25 prognosis-associated FRGs was conducted using the 'ConsensusClusterPlus' package in R software. The HPV negative TCGA-HNSC cohort was classified into three clusters at K=3 (Fig. 2A). Following this, UMAP was used to verify the accuracy of the clustering, which indicated that the three clusters were accurately distinguished at K=3 (Fig. 2B). The OS analysis revealed significant variations in prognoses among the three subgroups and cluster A had a favorable prognosis ($P=0.029$; Fig. 2C). The heatmap in Fig. 2D illustrates the expression of the FRGs and the respective clinicopathological features of the three clusters. For example, epidermal growth factor receptor (*EGFR*) was significantly upregulated in cluster B, and T3 stage. Furthermore, the transcription patterns of the FRGs in the three subgroups were depicted using boxplots. The expression levels of *EGFR* and transcription factor A, mitochondrial were markedly higher in cluster B than in clusters A and C, while the expression levels of NAD(P)H quinone dehydrogenase 1, *TRIB3*, glutamic-oxaloacetic transaminase 1, Sequestosome 1, CDGSH iron sulfur domain 1 and fumarate hydratase were higher in cluster C than in clusters A or B (Fig. 2E). Therefore, these differentially expressed FRGs may serve as important determinants for estimating the prognosis of patients with HNSCC, and based on their association with OS, they may be potentially useful therapeutic targets. The Kyoto Encyclopedia of Genes and Genomes (KEGG) pathway enrichment analysis performed using the GSEA package revealed different enrichment pathways between clusters A and B. This analysis was performed to identify significantly enriched pathways in clusters A and to clarify the unique activation or inhibition of metabolic, signal transduction, disease-related and other pathways in clusters A (Fig. 2F-I). Cluster A displayed significant involvement in critical pathways, such as 'KEGG_JAK_STAT_SIGNALING_PATHWAY',

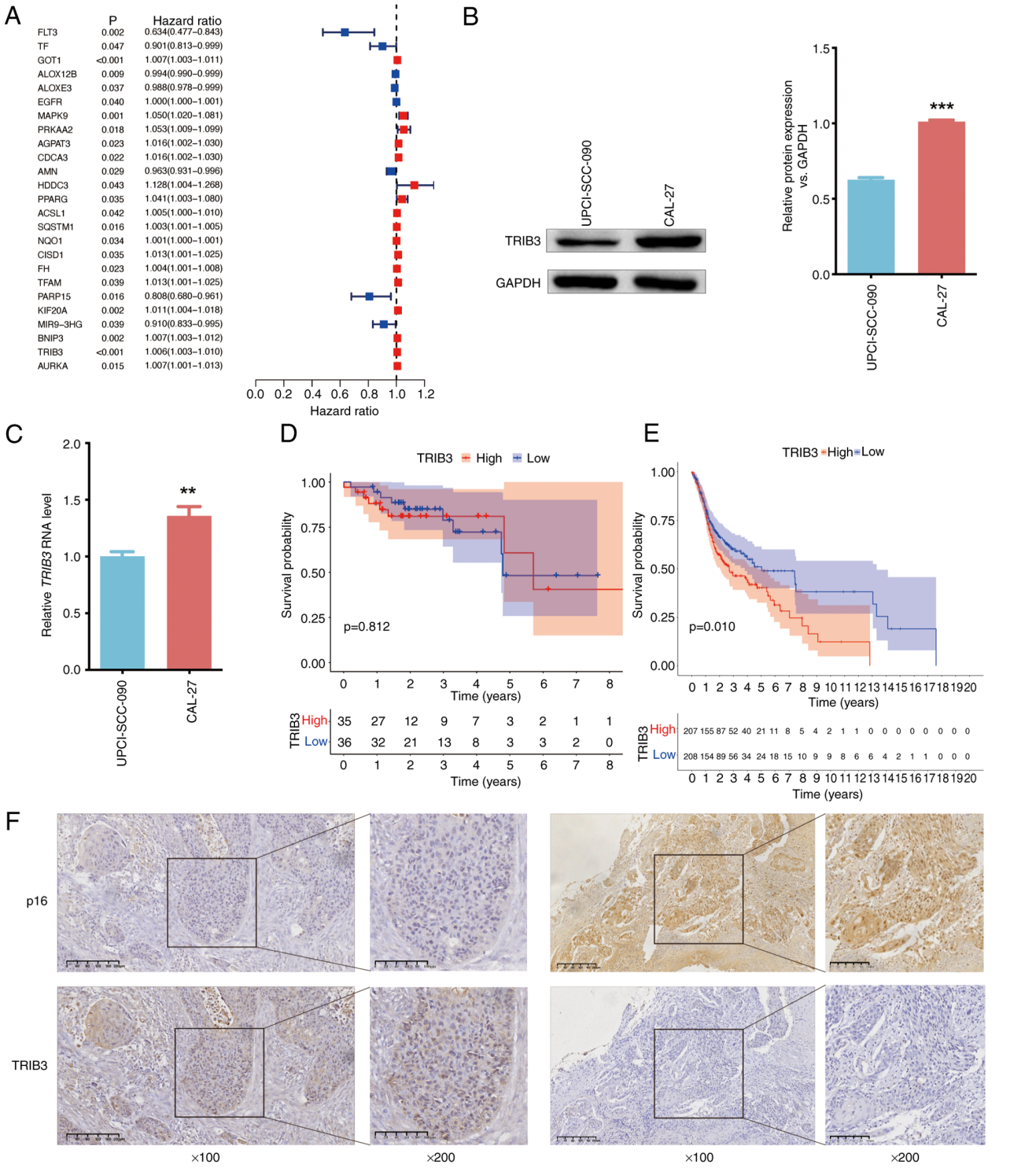

Figure 1. Analysis of prognosis-associated FRGs in TCGA-HNSC, the Kaplan-Meier survival analysis in patients with HPV-positive or negative HNSC (from the TCGA-HNSC dataset) and analysis of TRIB3 expression via cell culture and histological experiments. (A) The outcomes of the univariate Cox regression analysis of the TCGA-HNSC data conducted on the 25 FRGs are displayed in the forest plot. (B) TRIB3 protein expression in CAL27 (HPV-negative) and UPCI-SCC-090 (HPV-positive) cells was measured by western blotting. (C) The relative *TRIB3* mRNA expression in CAL27 (HPV-negative) and UPCI-SCC-090 (HPV-positive) cells was measured by reverse transcription-quantitative polymerase chain reaction. Kaplan-Meier survival analysis in TCGA-HNSC (D) HPV-positive and (E) HPV-negative patients. (F) TRIB3 protein expression in HPV-negative and HPV-positive paraffin-embedded samples was measured by immunohistochemistry. **P<0.01 and ***P<0.001. FRGs, ferroptosis related genes; HNSCC, head and neck squamous cell carcinoma; TCGA, The Cancer Genome Atlas; HPV, human papillomavirus; TRIB3, tribbles pseudokinase 3.

'KEGG_T_CELL_RECEPTOR_SIGNALING_PATHWAY', 'KEGG_GLUTATHIONE_METABOLISM' and 'KEGG_HEDGEHOG_SIGNALING_PATHWAY', all of which play essential roles in tumorigenesis.

Identification of prognostic FRG signatures using the FRG score model. The clinical utility of the 25 FRGs was evaluated using the LASSO-penalized Cox analysis (Fig. 3A and B). Following the core steps of LASSO Cox-based gene selection:

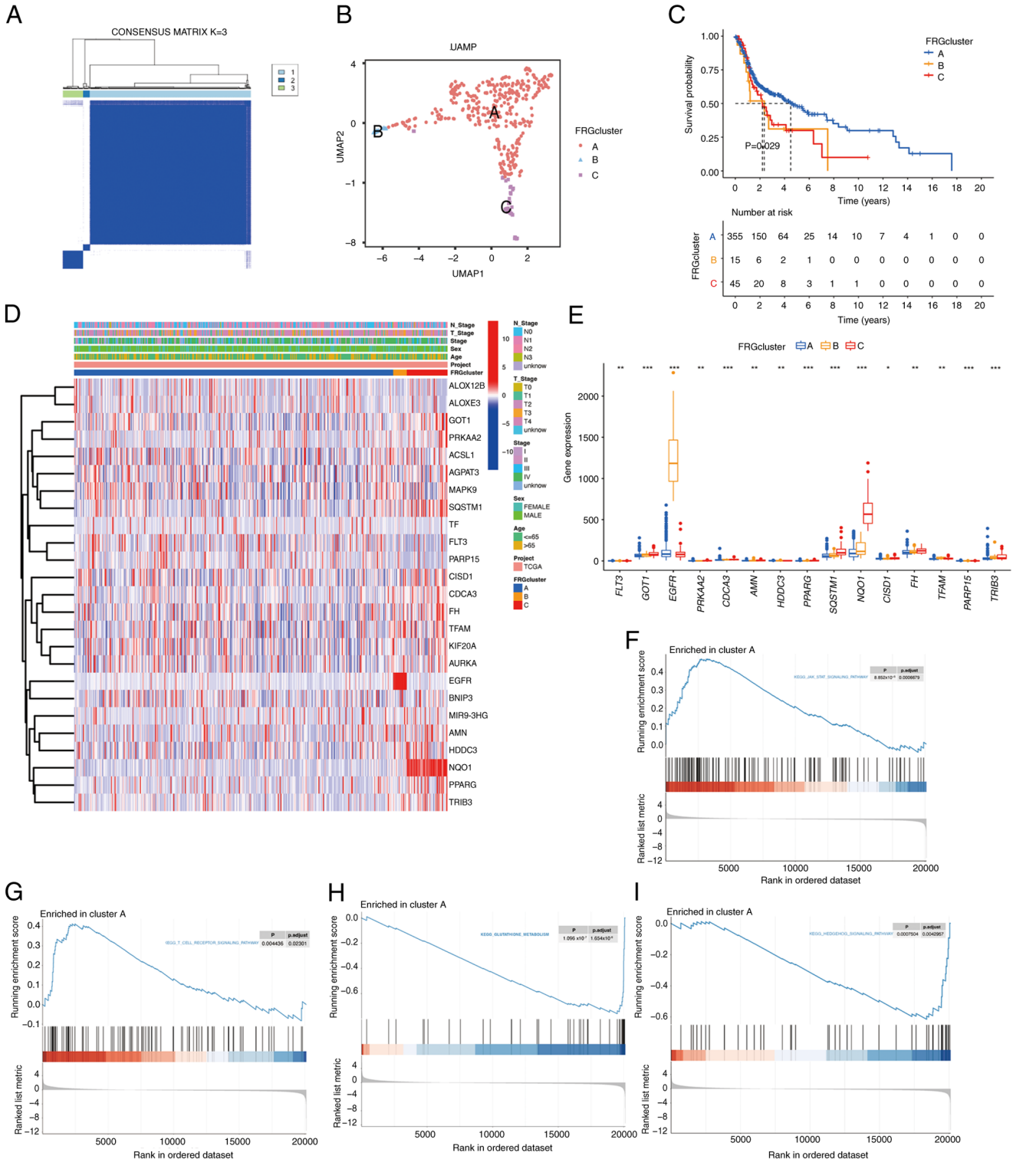

Figure 2. FRG-related subgroups of HPV-negative HNSCC samples from TCGA. (A) Consensus clustering. The consensus matrix of K=3 was obtained. (B) UMAP identified three clusters according to FRG expression. (C) Overall survival in the three clusters (P=0.029). (D) Heatmap of the clinicopathological characteristics and FRG expression associated with the three clusters. (E) The expression of FRGs in the three clusters. Comparative KEGG pathway enrichment between clusters A and B, as evaluated by GSEA. Cluster A displayed significant involvement in (F) KEGG_JAK_STAT_SIGNALING_PATHWAY, (G) KEGG_T_CELL_RECEPTOR_SIGNALING_PATHWAY, (H) KEGG_GLUTATHIONE_METABOLISM and (I) KEGG_HEDGEHOG_SIGNALING_PATHWAY. *P<0.05, **P<0.01, ***P<0.001. FRGs, ferroptosis related genes; HPV, human papillomavirus; HNSCC, head and neck squamous cell carcinoma; TCGA, The Cancer Genome Atlas; UMAP, Uniform Manifold Approximation and Projection; KEGG, Kyoto Encyclopedia of Genes and Genomes; GSEA, Gene Set Enrichment Analysis.

First, non-zero coefficient FRGs (that is FRGs contributing to survival prediction and free of multicollinearity) were initially extracted from the 25 candidates; second, these non-zero coefficient FRGs were further filtered by prioritizing those with larger absolute regression coefficients. In total, 10 prognostic FRGs, including *TRIB3*, *EGFR*, 1-acylglycerol-3-phosphate

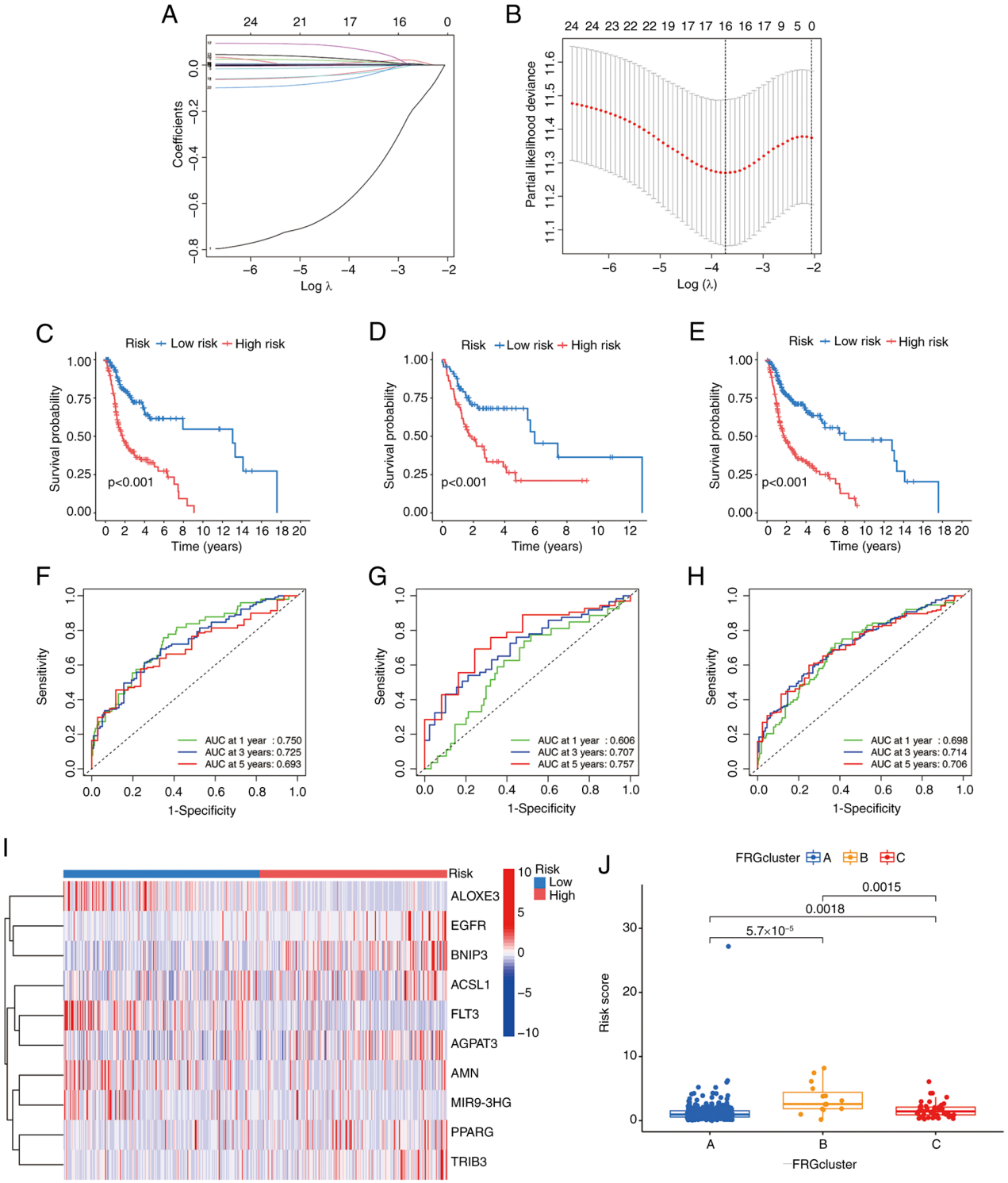

Figure 3. Determination of the prognostic FRGs in HPV-negative HNSCC samples from TCGA. (A) 10 prognostic FRGs were determined by the LASSO regression analysis and validated by 10-fold cross-validation. (B) The graph of the coefficient profile illustrated 10 prognostic FRGs. Kaplan-Meier survival curves showing the prognoses of the different risk groups in the (C) training, (D) testing and (E) combined cohorts. Time-dependent ROC curves were generated for OS at 1, 3 and 5 years using the (F) training, (G) testing and (H) combined cohorts. (I) The heatmap of the 10 hub FRGs for both risk groups. (J) Evaluation of the risk scores among the three previously established clusters. FRGs, ferroptosis related genes; TCGA, The Cancer Genome Atlas; LASSO, Least Absolute Shrinkage and Selection Operator; ROC, receiver operating characteristic; HPV, human papillomavirus; ALOXE3, lipoxygenase-3; EGFR, epidermal growth factor receptor; BNIP3, BCL2-interacting protein 3; ACSL1, acyl-CoA synthetase long chain family member 1; FLT3, FMS-like tyrosine kinase 3; AGPAT3, 1-acylglycerol-3-phosphate O-acyltransferase 3; AMN, amnion associated transmembrane protein; MIR9-3HG, MIR9-3 host gene; PPARG, peroxisome proliferator-activated receptor γ; TRIB3, tribbles pseudokinase 3.

O-acyltransferase 3 *(AGPAT3)*, peroxisome proliferator-activated receptor γ (*PPARG*), lipoxygenase-3 *(ALOXE3)*, BCL2-interacting protein 3 *(BNIP3)*, *ACSL1*, FMS-like tyrosine kinase 3 *(FLT3)*, amnion associated transmembrane protein *(AMN)* and MIR9-3 host gene *(MIR9-3HG)* were obtained from these 25 FRGs. The association coefficients are

presented in Table SIV, and the final risk score derived from the 10 FRG signatures is referred to as the 'FRGscore.' The prognostic index (FRGscore) was calculated according to the following formula: (0.00078 x *EGFR* expression) + (0.028 x *AGPAT3* expression) + (0.043 x *PPARG* expression) + (0.006 x *ACSL1* expression) + (0.007 x *BNIP3* expression) + (0.004 x *TRIB3* expression)-(0.02 x *ALOXE3* expression)-(0.798 x *FLT3* expression)-(0.05 x *AMN* expression)-(0.098 x *MIR9-3HG* expression). According to the FRGscore, the training, testing and combined cohorts were divided into high- and low-risk groups. Individuals or cases with scores above the median score were categorized as high-risk, and those below or equal to the median score as low-risk. The Kaplan-Meier survival curves indicated that the prognoses of the training, testing and combined cohorts in the high-risk group were poor (Fig. 3C-E). Using the FRGscore model, the time-dependent ROC curves exhibited notable predictive efficacy by evaluating OS at 1-, 3- and 5-year intervals. This was demonstrated by the AUC being >0.7, except the AUC at 1 year in the testing (0.606) and combined (0.698) cohorts (Fig. 3F-H). This supports the reliability of the predictive model for assessing the predefined outcomes. The heatmap shown in Fig. 3I illustrates the expression of the FRGs across various risk scores: *ALOXE3*, *FLT3*, *AMN* and *MIR903GH* showed greater expression levels in the high-risk group, whereas *EGFR*, *BNIP3*, *ACSL1*, *AGPAT3*, *PPARG* and *TRIB3* exhibited higher expression in the low-risk group. Additionally, the risk scores of the previously established three clusters varied significantly from each other (Fig. 3J).

Development of a prognostic nomogram for patients with HPV-negative HNSCC. For the nomogram integrating FRGscore and clinical data, the impact of clinicopathological variables was considered by first screening prognosis-related variables (such as age and tumor stage) via univariate Cox regression, then validating their independent prognostic value by multivariate Cox regression and including significant variables (P<0.05) together with FRGscore, and finally assigning each variable a prognostic weight-based score scale to quantify contributions for multi-dimensional outcome prediction (Fig. 4A). The accuracy of the nomogram was verified through a calibration curve (Fig. 4B). DCA determines the possible patient benefit of clinical prediction models, diagnostic procedures and molecular markers (35). The reliability of the nomogram for estimating the short- and long-term survival of patients with HNSCC was confirmed by the DCA (Fig. 4C-E). The multivariable Cox regression analysis showed that the primary influencing factors in the nomogram were sex, N stage and risk score (Fig. 4F). The constructed nomogram may thus be valuable for the prediction of clinical prognosis.

Immune infiltration in patients with HPV-negative HNSCC. Both tumor progression and the efficacy of immunotherapy are influenced by the IME. To distinguish between the risk groups of patients with HPV-negative HNSCC, the tumor IME was investigated in more detail. The CIBERSORT R script was used to assess the percentages of infiltrating immune cell types. HPV-negative HNSCC tumors were ranked based on the risk score, and associations between the immune cell types and risk scores were observed (Fig. 5A). The low-risk group represented a higher proportion of T cells, B cells and NK cells, whereas the high-risk group represented a higher proportion of macrophages, mast cells, eosinophils and neutrophils. The correlations among immune cells in patients with HNSCC are displayed in Fig. 5B. T cells CD4 memory activated was positively associated with T cells CD8 (r=0.58), while T cells CD8 was negatively associated with macrophages M0 (r=-0.53). This may provide insights into the specific IME associated with certain tumor types. In patients with low-risk HNSCC without HPV infection, M0 macrophages accounted for a lower proportion of immune cell components, as well as $CD8^+$ T cells, T cells CD4 memory activated, NK cells resting and mast cells activated (Fig. 5C).

Subsequently, the stromal and immune scores for both risk groups were determined using the estimated score of the expression profile. The core purpose of calculating stromal and immune scores for both risk groups is to link the 'FRGscore-based molecular risk stratification' with 'tumor microenvironment characteristics', which not only provides TME-level support for the mechanism by which FRGscore affects prognosis but also offers a basis for formulating subsequent intervention strategies (such as immunotherapy) for different risk groups. The StromalScore, ImmuneScore and ESTIMATEScore represented a significant difference between the high-risk and low-risk groups (Fig. 5D). Furthermore, the infiltration of various immune cell types was relatively significantly correlated with the 10 FRGs that were used to develop the FRGscore model (Fig. 5E). Elevated risk scores were linked to a greater number of M0 macrophages (P=0.29; Fig. 5F) but fewer $CD8^+$ T cells (P=-0.2; Fig. 5G). Furthermore, there was notable variation in the extent of immune cell infiltration across the three FRG clusters (Fig. 5H). Cluster B showed fewer activated CD8 cells, MDSCs, mast cells, type 1 T helper cells and type 2 T helper cells than the other two clusters, while cluster C showed fewer activated B cells, activated CD4 T cells, gd T, immature B cells, natural killer T cells, neutrophils, plasmacytoid dendritic cells, regulatory T cells and type 17 T helper cells. The 'pRRophetic' package in R was used to assess therapeutic drug susceptibility in the different risk groups. A significant association was observed between the risk score and the responsiveness to various drugs, for example, samples with high risk were more sensitive to the two drugs sorafenib and lapatinib (Fig. 5I and J).

TRIB3 knockdown induces ferroptosis in HPV-negative HNSCC cells. To determine whether *TRIB3* mediated ferroptosis in HPV-negative HNSCC cells, *TRIB3* was knocked down in CAL27 cells using three different siRNA sequences. RT-qPCR revealed that *TRIB3* mRNA expression significantly decreased after *TRIB3* siRNA transfection (Fig. 6A), indicating successful *TRIB3* knockdown in CAL27 cells. Transfection with *TRIB3* siRNA-3 induced the largest effect. Therefore, *TRIB3* siRNA-3 was selected for further studies. The cellular content of Fe^{2+}, GSH and MDA, which can reflect the ferroptosis state, were quantified, while the level of ROS (another indicator of ferroptosis) was visualized via imaging; these analyses were performed to investigate whether TRIB3 inhibits ferroptosis in HNSCC cells. Upon *TRIB3* knockdown in cancer cells (CAL27), the concentration of GSH decreased (Fig. 6B), while the concentrations of Fe^{2+} and MDA increased (Fig. 6C and D). Furthermore,

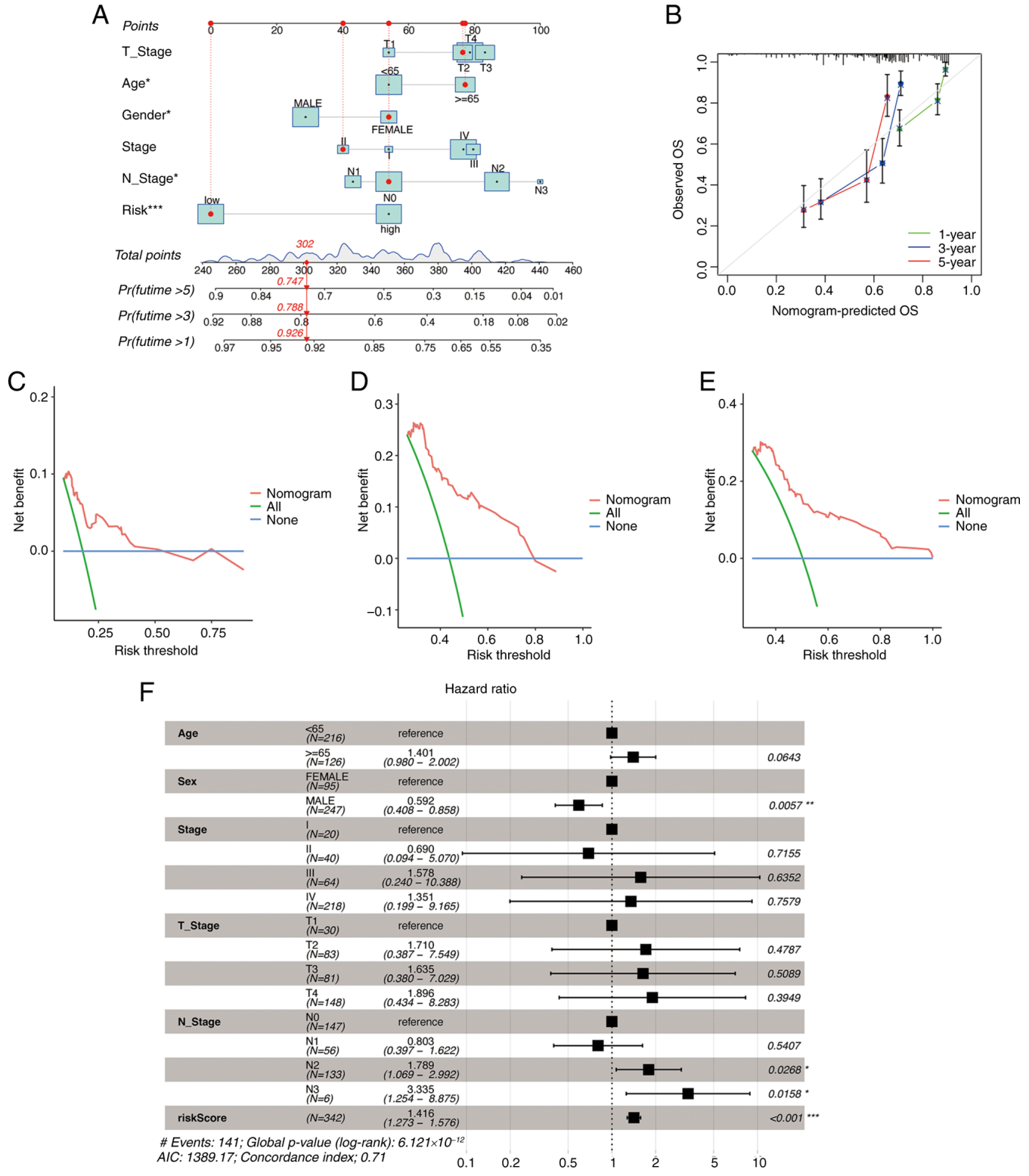

Figure 4. Nomogram for patients with HPV-negative HNSCC samples from TCGA. (A) The nomogram was constructed based on the clinicopathological variables and ferroptosis-related gene risk scores. (B) Calibration curve for nomogram validation. Decision curves of the nomogram at (C) 1-year, (D) 3-year and (E) 5-year intervals. (F) Forest plot showing the multivariable Cox regression analysis of clinical features and the risk scores for patients with HPV-negative HNSCC. *P<0.05, **P<0.01, ***P<0.001. HNSCC, head and neck squamous cell carcinoma; HPV, human papillomavirus; OS, overall survival.

intracellular ROS were upregulated after *TRIB3* knockdown, indicating ferroptosis induction (Fig. 6E). Moreover, in CAL27 cells with siRNA, transmission electron microscopy elucidated a discernible decrease or complete absence of mitochondrial ridges, concomitant with elevated mitochondrial membrane density (Fig. 6F). Finally, cell cycle analysis was performed by flow cytometry, indicating that *TRIB3* knockdown decreased the population of cells in the S phase (Fig. 6G). These findings suggest that *TRIB3* knockdown may promote ferroptosis in HPV-negative HNSCC cells.

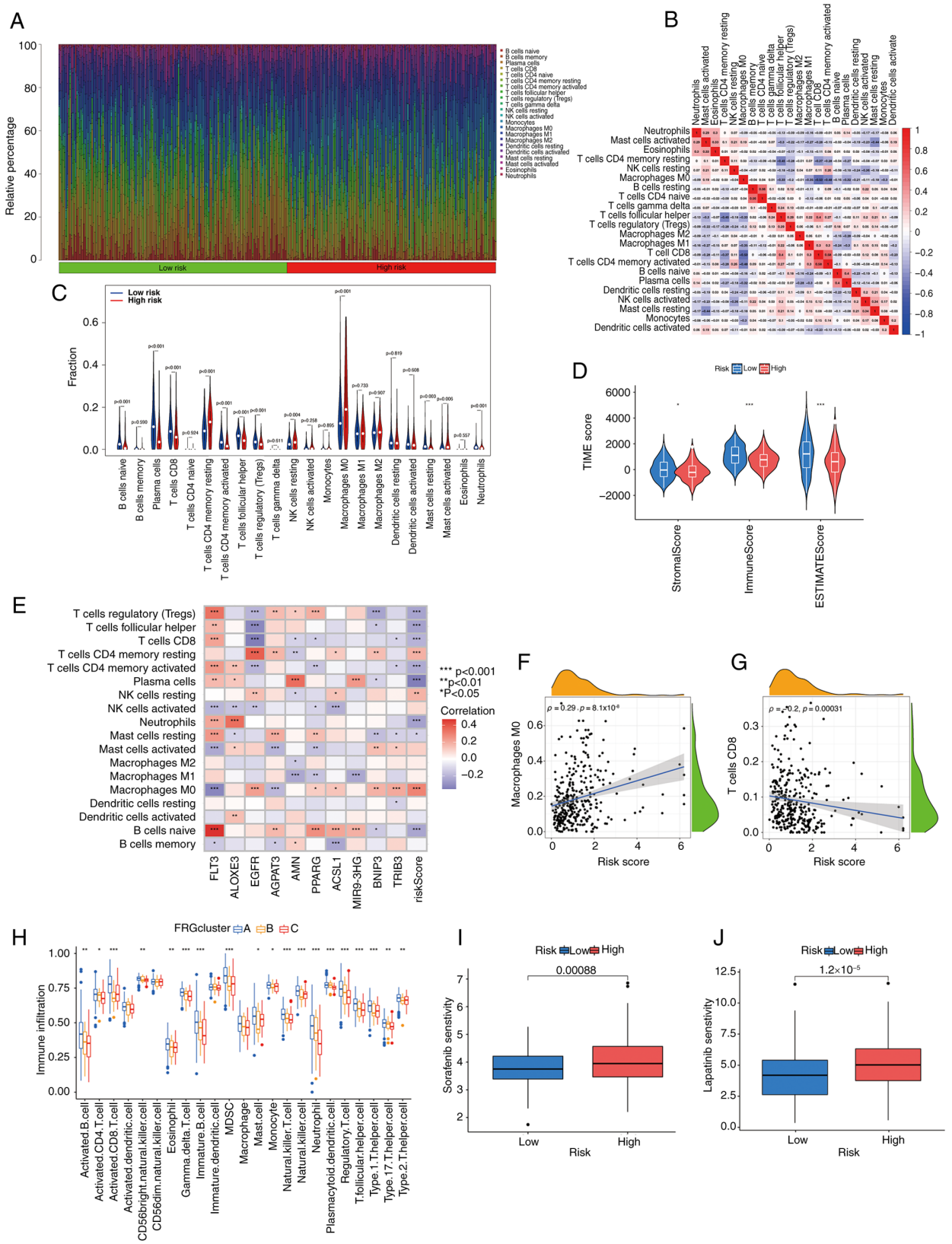

Figure 5. Exploring the immune microenvironment of HPV-negative HNSCC based on the various risk scores and clusters in HPV-negative HNSCC samples from TCGA. (A) Different proportions of infiltrating immune cells with distinct risk scores. (B) The associations among immune cells. (C) Comparison of immune cell components between the risk groups. (D) The predicted score of the gene expression patterns in both risk groups. (E) The connection between immune cells and the 10 main ferroptosis-related genes. Associations of (F) the number of M0 macrophages and (G) the number of $CD8^+$ T cells in HNSCC-negative tissues with risk scores. (H) The variation in the extent of immune cell infiltration across the three FRG clusters. The susceptibility of both risk groups to (I) sorafenib and (J) lapatinib. *P<0.05, **P<0.01, ***P<0.001. HNSCC, head and neck squamous cell carcinoma; HPV, human papillomavirus; TCGA, The Cancer Genome Atlas; TME, tumor microenvironment; FRG, ferroptosis related gene; FLT3, FMS-like tyrosine kinase 3; ALOXE3, lipoxygenase-3; EGFR, epidermal growth factor receptor; AGPAT3, 1-acylglycerol-3-phosphate O-acyltransferase 3; AMN, amnion associated transmembrane protein; PPARG, peroxisome proliferator-activated receptor γ; ACSL1, acyl-CoA synthetase long chain family member 1; MIR9-3HG, MIR9-3 host gene; BNIP3, BCL2-interacting protein 3; TRIB3, tribbles pseudokinase 3.

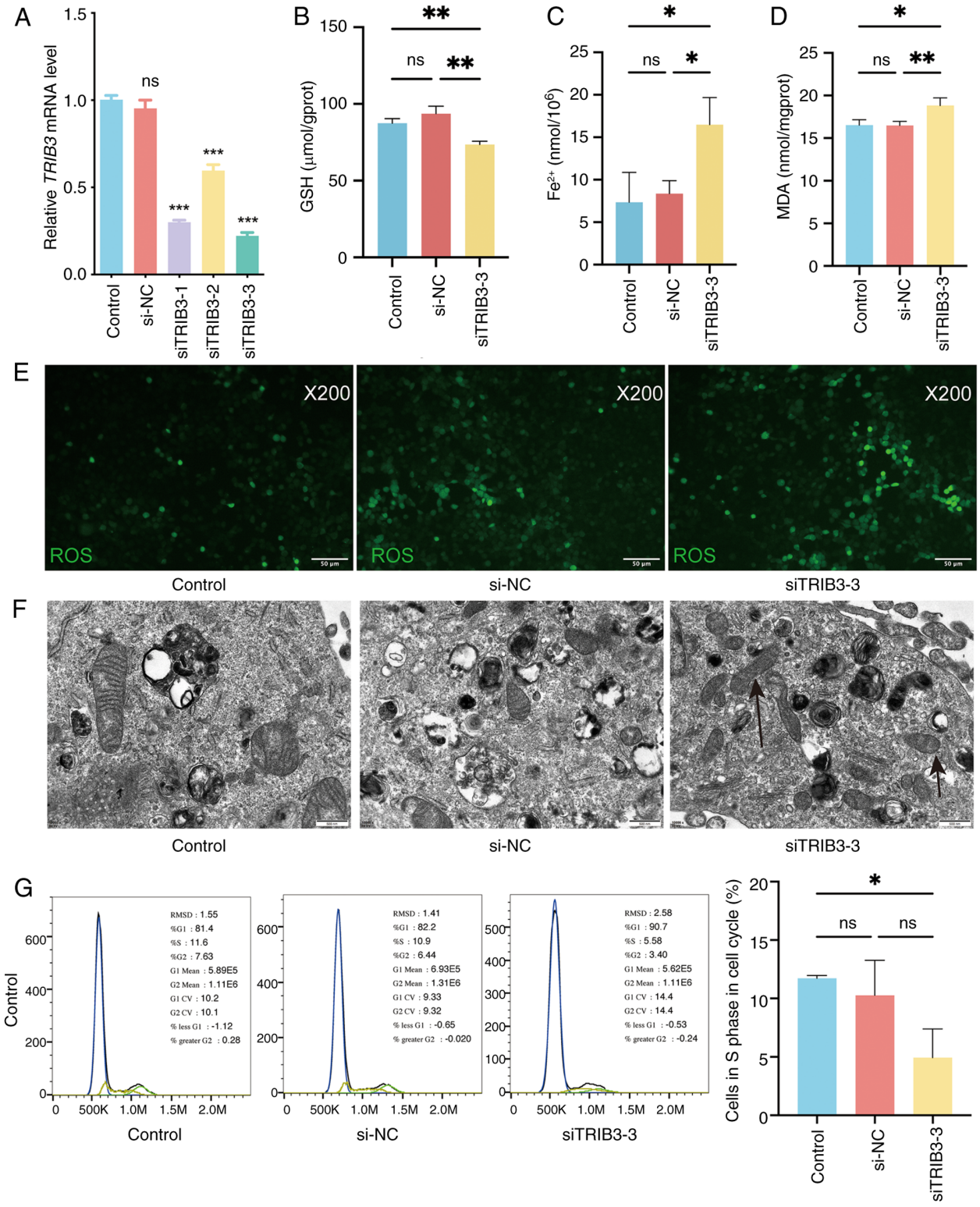

Figure 6. Knockdown of *TRIB3* promotes ferroptosis in HPV-negative HNSCC cells. (A) Relative *TRIB3* mRNA expression in CAL27 cells in the different groups measured by reverse transcription-quantitative polymerase chain reaction after siRNA transfection. (B) The intracellular GSH concentration was measured using the reduced GSH Colorimetric Assay Kit. (C) The intracellular Fe^{2+} concentration was measured using the Cell Ferrous Iron Colorimetric Assay Kit. (D) The intracellular MDA concentration was measured using the Cell Malondialdehyde Colorimetric Assay Kit. (E) ROS (green fluorescence) were measured in the cells. (F) Observation of the cells under transmission electron microscopy. (G) Cell cycle distribution analysis using flow cytometry. *P<0.05, **P<0.01, ***P<0.001. ns, non-significant; HNSCC, head and neck squamous cell carcinoma; GSH, glutathione; MDA, malondialdehyde; ROS, reactive oxygen species; HPV, human papillomavirus; TRIB3, tribbles pseudokinase 3; si, small interfering (RNA); NC, negative control.

TRIB3 overexpression inhibits ferroptosis in HPV-positive HNSCC cells. To determine whether *TRIB3* mediates ferroptosis in HPV-positive HNSCC cells, *TRIB3* was overexpressed in UPCI-SCC-090 cells. RT-qPCR revealed that *TRIB3* mRNA expression significantly increased after *TRIB3* transfection (Fig. 7A), indicating successful *TRIB3* overexpression

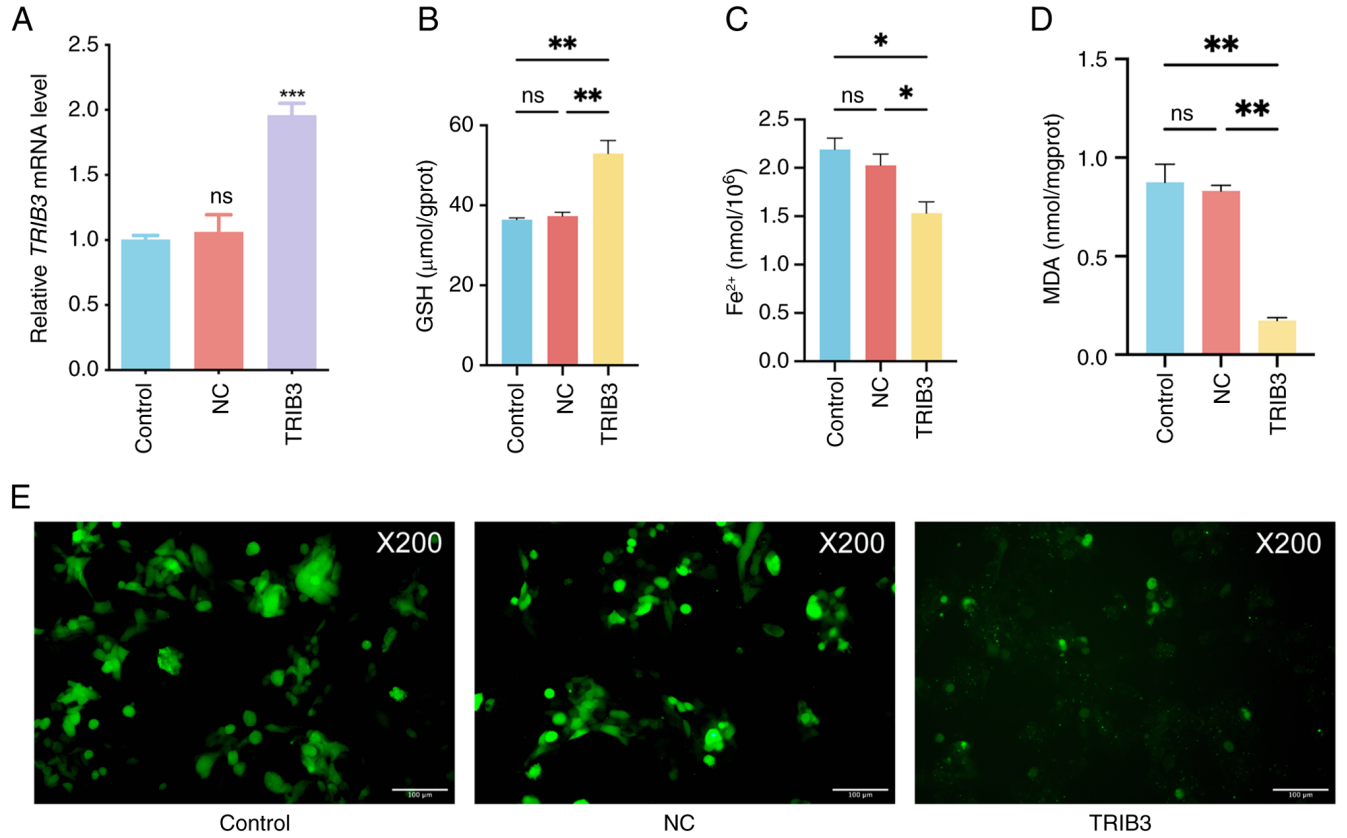

Figure 7. *TRIB3* overexpression inhibits ferroptosis in HPV-positive HNSCC cells. (A) Relative *TRIB3* mRNA expression in the different groups measured by reverse transcription-quantitative polymerase chain reaction. (B) The intracellular GSH concentration was measured using the reduced GSH Colorimetric Assay Kit. (C) The intracellular Fe^{2+} concentration was measured using the Cell Ferrous Iron Colorimetric Assay Kit. (D) The intracellular MDA concentration was measured using the Cell Malondialdehyde Colorimetric Assay Kit. (E) ROS (green fluorescence) were measured in the cells. *P<0.05, **P<0.01, ***P<0.001. ns, non-significant; HPV, human papillomavirus; HNSCC, head and neck squamous cell carcinoma; GSH, glutathione; MDA, malondialdehyde; ROS, reactive oxygen species; TRIB3, tribbles pseudokinase 3; NC, negative control.

in UPCI-SCC-090 cells. Furthermore, the concentrations of Fe^{2+}, GSH and MDA were quantified while the level of ROS was visualized via imaging; these analyses were conducted to assess the potential induction of ferroptosis by TRIB3 in HPV-positive HNSCC cells. TRIB3 overexpression in HPV positive HNSCC cancer cells (UPCI-SCC-090) led to an increase in the GSH concentration (Fig. 7B), accompanied by a decrease in the Fe^{2+} and MDA concentrations (Fig. 7C and D). Moreover, there was a noticeable decline in intracellular ROS following TRIB3 overexpression, indicating ferroptosis suppression (Fig. 7E). These results suggest that TRIB3 expression may inhibit ferroptosis in HPV-positive HNSCC cells.

Discussion

Ferroptosis is a unique form of cell death (23) and a previous study demonstrated an association between ferroptosis and HNC treatment: In murine models, ferroptosis inducers and specific antitumor drugs, such as cisplatin, have shown synergistic effects in suppressing the progression of HNC (25). Although a number of studies have compared FRGs between healthy tissues and HNSCC tissues (31,32), the differences in FRG expression between HPV-positive and HPV-negative HNSCC have not yet been well reported. However, it has been demonstrated that HPV16 integration confers ferroptosis resistance in cervical squamous cell carcinoma via the c-Myc/microRNA-142-5p/Homeobox A5/solute carrier family 7 member 11 axis (39). Additionally, HPV status has been identified as a key determinant of ferroptosis sensitivity in HNSCC, with HPV E6/E7 interfering with NFE2-like BZIP transcription factor 2 pathways in HPV-positive cases and HPV-negative HNSCC relying more on glutathione peroxidase 4-dependent defense (40). Additionally, a cross-tumor analysis has confirmed distinct ferroptosis-related metabolic signatures between HPV subtypes, including enhanced ROS detoxification in HPV-positive HNSCC and pro-oxidative pathways with immune suppression in HPV-negative patients (41). Collectively, these findings, from the mechanistic regulation of ferroptosis by HPV oncogenes and the subtype-specific ferroptosis sensitivity mediated by HPV status, to the distinct ferroptosis-related metabolic profiles, provide compelling evidence that FRG expression differs between HPV-positive and HPV-negative HNSCC, highlighting the necessity of stratifying HNSCC by HPV status when investigating ferroptosis-associated mechanisms and therapeutic strategies.

In the present study, the expression of FRGs in HPV-positive and HPV-negative HNSCC were investigated, given the known biological differences between these two subtypes of HNSCC, specifically in terms of etiopathogenesis, molecular genetic characteristics, clinicopathologic presentation and prognosis (5). To develop a prognostic model for the HPV-negative

group, 10 FRGs were specifically identified (*ALOXE3*, *ACSL1*, *TRIB3*, *FLT3*, *EGFR*, *AGPAT3*, *AMN*, *PPARG*, *MIR9-3HG* and *BNIP3*) as per their efficacy in the LASSO Cox regression analysis. According to the findings, this model could function as a reliable prognostic indicator for patients with HPV-negative HNSCC. Furthermore, the RT-qPCR, western blotting and immunohistochemistry analyses performed in the present study demonstrated that among the 10 FRGs, *TRIB3* exhibited higher expression in HPV-negative samples than in HPV-positive samples.

TRIB3, which belongs to the Tribbles-related family, has been found to have biological associations with a range of cancer types including oral squamous cell carcinoma, breast cancer, lung adenocarcinoma, renal cell carcinoma, colorectal cancer and glioblastoma, and it can act as either an oncogene or a tumor suppressor (42-47). *TRIB3* is involved in various biological processes, including lipid and glucose metabolism, epithelial-to-mesenchymal transition, cell proliferation, differentiation and the cellular stress response (46,48,49). As lipid peroxidation and iron overload are the main metabolic characteristics of ferroptosis (50), whether *TRIB3* regulated ferroptosis in HPV-positive and HPV-negative cells was evaluated in the present study. It was found that *TRIB3* knockdown impeded the survival of HPV-negative HNSCC cells. Moreover, *TRIB3* knockdown led to elevated intracellular Fe^{2+}, MDA and ROS levels, along with a decrease in GSH. Conversely, TRIB3 overexpression in HPV-positive HNSCC cells yielded contrasting outcomes. Additionally, after *TRIB3* knockdown, transmission electron microscopy revealed a notable reduction or complete loss of mitochondrial ridges, along with a notable increase in mitochondrial membrane density. The downregulation of *TRIB3* resulting in the occurrence of ferroptosis in HPV-negative HNSCC cells was thus highlighted by the results of the present study. *TRIB3* may become a new target that can trigger ferroptosis in both HPV-positive and HPV-negative cancer cells. Nevertheless, further investigation is necessary to understand the mechanism by which *TRIB3* influences ferroptosis. Additionally, in the present study, the Kaplan-Meier analysis and prognostic model demonstrated that *TRIB3* had a more significant clinical impact in patients with HPV-negative HNSCC compared with HPV-positive. Furthermore, compared with HPV-positive HNSCC cells, TRIB3 expression is upregulated in HPV-negative HNSCC. Given the biological disparities between these two subtypes, the upregulation of TRIB3 is not merely a quantitative elevation, but rather a qualitative alteration intimately linked to their distinct oncogenic drivers and regulatory mechanisms, which implies that multiple distinct pathways may underlie this upregulation and, in turn, modulate ferroptosis. Finally, despite TRIB3 mediating ferroptosis in both HPV-positive and HPV-negative HNSCC cells, the underlying mechanism of this effect remains unknown. Whether *TRIB3* functions through the same pathway in these two subtypes of HNSCC requires further investigation.

Aside from *TRIB3,* the prognostic model constructed in the present study included 9 other genes: *EGFR*, *AGPAT3*, *PPARG*, *ACSL1*, *BNIP3*, *ALOXE3*, *FLT3*, *AMN* and *MIR9-3HG*. *EGFR*, a promoter of HNSCC growth and development, is upregulated in >90% of cases of HNSCC (51). Moreover, EGFR reduces N6-methyladenosine and protects against ferroptosis in glioblastoma by promoting ALKBH5 nuclear retention (52). *ACSL1*, which encodes an essential enzyme involved in the modulation of lipid metabolism, increases ferroptosis resistance and antioxidant capacity in ovarian cancer by regulating the myristoylation of AIF family member 2 (53). ACSL1 was also observed to be upregulated in HPV-negative HNSCC in the present study; however, to the best of our knowledge, no studies have yet investigated the relationship between ACSL1 and HPV infection. In addition, *ALOXE3,* a YAP-TEAD target gene, is associated with YAP-induced ferroptosis and significantly increases the risk of death induced by ferroptosis in hepatocellular carcinoma cells when overexpressed (54). *PPARG*, which encodes a nuclear receptor associated with the modulation of lipid metabolism, mediates the ferroptosis of dendritic cells, limiting antitumor immunity in mice (55). Moreover, research on *FLT3*-mediated ferroptosis is primarily focused on *FLT3*-mutant leukemia (56,57). Bioinformatics analyses have also reported that *BNIP3*, *AMN* and *MIR9-3HG* are involved in ferroptosis during carcinogenesis (58-60). However, there is currently no research on *AGPAT3* and its role in mediating ferroptosis, making this a novel finding of the present study.

The immune system modulates the response to therapy and inhibits tumor growth, invasion and metastasis. Immune surveillance provides a method for identifying, controlling and eliminating tumor cells (27-29). Lipid mediators may be generated by ferroptotic cells as recognition signals to recruit antigen-presenting cells and other immune cells into the microenvironment of the ferroptosis tumor (61). However, the relationship between infiltrating immune cells and ferroptosis in HNSCC remains unclear. In the present study, increased infiltrating immune cells, such as quiescent dendritic cells, plasma cells, mast cells, regulatory T cells and naïve B cells, were found in the low-risk group, while the high-risk group demonstrated elevated infiltration of neutrophils, activated $CD4^+$ T cells and mast cells. Moreover, a significant correlation was observed among the 10 hub FRGs, the risk score and various immune cell types. Thus, these 10 FRGs may induce ferroptosis and thus regulate immunological therapy, positioning them as potential new targets in patients with HPV-negative HNSCC. However, even when the scale of the confirmation has been estimated, CIBERSORT predictions remain limited. This is because deconvolution of bulk RNA-sequencing data can be noisy, an issue that is particularly pronounced in heterogeneous tumors. Experimental verification is needed to confirm these results, and such validation could first extend to prospective multicenter cohorts of patients with HPV-negative HNSCC to verify the robustness of the 10-FRG-based prognostic model across diverse populations, addressing the current reliance on retrospective TCGA data.

The present study has some limitations that should be considered. First, the prognostic model was developed by analyzing publicly available datasets. Therefore, the findings still require verification in prospective multicenter cohorts. Second, the *in vitro* validation of TRIB3, was limited to single HPV-negative (CAL27) and HPV-positive (UPCI-SCC-090) HNSCC cell lines, risking biological variability-related confounding factors. These results will be followed by experiments expanding the cell panel to additional HPV-negative (such as SCC-25 and HN6) and HPV-positive (such as SCC-47) cell lines and incorporating patient-derived primary cells to verify the function of TRIB3 and reduce variability. Third, only

TRIB3, one of the risk signature genes, was evaluated *in vitro*. More studies are required to evaluate the functions of *EGFR*, *AGPAT3*, *PPARG*, *ACSL1*, *BNIP3*, *ALOXE3*, *FLT3*, *AMN* and *MIR9-3HG* in the pathogenesis and development of HNSCC. Moreover, studying the mechanisms by which the identified FRGs regulate ferroptosis is essential for comprehending their roles and potential implications in cellular functions and disease processes. Last, the present study is limited by the absence of *in vivo* data. Given that *in vivo* validation is critical to verifying the biological function of a target gene and evaluating its clinical translation potential, future work should prioritize investigating the function of TRIB3 in *in vivo* models to confirm its utility for clinical translation.

In conclusion, the present study identified 10 hub genes associated with ferroptosis, including *TRIB3*, *EGFR*, *AGPAT3*, *PPARG*, *ACSL1*, *BNIP3*, *ALOXE3*, *FLT3*, *AMN* and *MIR9-3HG*. A prognostic model was developed for the HPV-negative patient group using these 10 hub FRGs. Thus, these 10 FRGs may serve as prognostic markers for patients with HPV-negative HNSCC. *TRIB3* expression was higher in HPV-negative clinical samples than in HPV-positive clinical samples. *TRIB3* knockdown resulted in increased intracellular Fe^{2+}, MDA and ROS, reduced GSH and the diminishment or absence of mitochondrial ridges in HPV-negative HNSCC cells. Conversely, *TRIB3* overexpression resulted in decreased intracellular Fe^{2+}, MDA and ROS, but increased GSH in HPV-positive HNSCC cells. These results indicate a novel association between *TRIB3* and ferroptosis in both HPV-positive and -negative HNSCC cells. *TRIB3* had a more significant clinical impact in the HPV-negative HNSCC group than in the HPV-positive HNSCC group, thereby providing a direction to improve clinical outcomes for patients with HPV-negative HNSCC.

Acknowledgements

Not applicable.

Funding

No funding was received.

Availability of data and materials

The data generated in the present study may be requested from the corresponding author.

Authors' contributions

JL, NAR, SM and GY were responsible for conception. JL and GY performed the interpretation and analysis of data. JL prepared the manuscript. JL, NAR, SM and GY revised the manuscript for important intellectual content. The study was supervised by GY. JL and GY confirm the authenticity of all the raw data. All authors have read and approved the final version of the manuscript.

Ethics approval and consent to participate

Ethical approval for this retrospective study using de-identified data was granted by the Human Ethical Committee of Heping Hospital Affiliated to Changzhi Medical College [Changzhi, China; approval no. 2023(027)]. The committee also waived the requirement for informed consent.

Patient consent for publication

Not applicable.

Competing interests

The authors declare that they have no competing interests.

References

1. Reid PA, Wilson P, Li Y, Marcu LG and Bezak E: Current understanding of cancer stem cells: Review of their radiobiology and role in head and neck cancers. Head Neck 39: 1920-1932, 2017.
2. Sung H, Ferlay J, Siegel RL, Laversanne M, Soerjomataram I, Jemal A and Bray F: Global cancer statistics 2020: GLOBOCAN estimates of incidence and mortality worldwide for 36 cancers in 185 countries. CA Cancer J Clin 71: 209-249, 2021.
3. Johnson DE, Burtness B, Leemans CR, Lui VWY, Bauman JE and Grandis JR: Head and neck squamous cell carcinoma. Nat Rev Dis Primers 6: 92, 2020.
4. Mody MD, Rocco JW, Yom SS, Haddad RI and Saba NF: Head and neck cancer. Lancet 398: 2289-2299, 2021.
5. Chi AC, Day TA and Neville BW: Oral cavity and oropharyngeal squamous cell carcinoma-an update. CA Cancer J Clin 65: 401-421, 2015.
6. Wuerdemann N, Wittekindt C, Sharma SJ, Prigge ES, Reuschenbach M, Gattenlöhner S, Klussmann JP and Wagner S: Risk factors for overall survival outcome in surgically treated human Papillomavirus-Negative and positive patients with oropharyngeal cancer. Oncol Res Treat 40: 320-327, 2017.
7. Yu W, Chen Y, Putluri N, Osman A, Coarfa C, Putluri V, Kamal AHM, Asmussen JK, Katsonis P, Myers JN, *et al*: Evolution of cisplatin resistance through coordinated metabolic reprogramming of the cellular reductive state. Br J Cancer 128: 2013-2024, 2023.
8. Azharuddin M, Roberg K, Dhara AK, Jain MV, Darcy P, Hinkula J, Slater NKH and Patra HK: Dissecting multi drug resistance in head and neck cancer cells using multicellular tumor spheroids. Sci Rep 9: 20066, 2019.
9. Hu H, Li B, Wang J, Tan Y, Xu M, Xu W and Lu H: New advances into cisplatin resistance in head and neck squamous carcinoma: Mechanisms and therapeutic aspects. Biomed Pharmacother 163: 114778, 2023.
10. Mackenzie IC: Stem cell properties and epithelial malignancies. Eur J Cancer 42: 1204-1212, 2006.
11. Norouzi A, Liaghat M, Bakhtiyari M, Noorbakhsh Varnosfaderani SM, Zalpoor H, Nabi-Afjadi M and Molania T: The potential role of COVID-19 in progression, chemo-resistance, and tumor recurrence of oral squamous cell carcinoma (OSCC). Oral Oncol 144: 106483, 2023.
12. Kang SH, Oh SY, Lee KY, Lee HJ, Kim MS, Kwon TG, Kim JW, Lee ST, Choi SY and Hong SH: Differential effect of cancer-associated fibroblast-derived extracellular vesicles on cisplatin resistance in oral squamous cell carcinoma via miR-876-3p. Theranostics 14: 460-479, 2024.
13. Usman S, Waseem NH, Nguyen TKN, Mohsin S, Jamal A, The MT and Waseem A: Vimentin is at the heart of epithelial mesenchymal transition (EMT) mediated metastasis. Cancers (Basel) 13: 4985, 2021.
14. Gong Y, Fan Z, Luo G, Yang C, Huang Q, Fan K, Cheng H, Jin K, Ni Q, Yu X and Liu C: The role of necroptosis in cancer biology and therapy. Mol Cancer 18: 100, 2019.
15. Hsu SK, Li CY, Lin IL, Syue WJ, Chen YF, Cheng KC, Teng YN, Lin YH, Yen CH and Chiu CC: Inflammation-related pyroptosis, a novel programmed cell death pathway, and its crosstalk with immune therapy in cancer treatment. Theranostics 11: 8813-8835, 2021.
16. Liu J, Kuang F, Kang R and Tang D: Alkaliptosis: A new weapon for cancer therapy. Cancer Gene Ther 27: 267-269, 2020.
17. Tong X, Tang R, Xiao M, Xu J, Wang W, Zhang B, Liu J, Yu X and Shi S: Targeting cell death pathways for cancer therapy: Recent developments in necroptosis, pyroptosis, ferroptosis, and cuproptosis research. J Hematol Oncol 15: 174, 2022.

18. Zhang C, Liu X, Jin S, Chen Y and Guo R: Ferroptosis in cancer therapy: A novel approach to reversing drug resistance. Mol Cancer 21: 47, 2022.
19. Dixon SJ, Lemberg KM, Lamprecht MR, Skouta R, Zaitsev EM, Gleason CE, Patel DN, Bauer AJ, Cantley AM, Yang WS, *et al*: Ferroptosis: An iron-dependent form of nonapoptotic cell death. Cell 149: 1060-1072, 2012.
20. Xie Y, Hou W, Song X, Yu Y, Huang J, Sun X, Kang R and Tang D: Ferroptosis: Process and function. Cell Death Differ 23: 369-379, 2016.
21. Conrad M and Pratt DA: Publisher correction: The chemical basis of ferroptosis. Nat Chem Biol 16: 223-224, 2020.
22. Stockwell BR: Ferroptosis turns 10: Emerging mechanisms, physiological functions, and therapeutic applications. Cell 185: 2401-2421, 2022.
23. Xue Y, Jiang X, Wang J, Zong Y, Yuan Z, Miao S and Mao X: Effect of regulatory cell death on the occurrence and development of head and neck squamous cell carcinoma. Biomark Res 11: 2, 2023.
24. Kim EH, Shin D, Lee J, Jung AR and Roh JL: CISD2 inhibition overcomes resistance to sulfasalazine-induced ferroptotic cell death in head and neck cancer. Cancer Lett 432: 180-190, 2018.
25. Roh JL, Kim EH, Jang HJ, Park JY and Shin D: Induction of ferroptotic cell death for overcoming cisplatin resistance of head and neck cancer. Cancer Lett 381: 96-103, 2016.
26. Ye J, Jiang X, Dong Z, Hu S and Xiao M: Low-Concentration PTX And RSL3 inhibits tumor cell growth synergistically by inducing ferroptosis in mutant p53 hypopharyngeal squamous carcinoma. Cancer Manag Res 11: 9783-9792, 2019.
27. Dersh D, Hollý J and Yewdell JW: A few good peptides: MHC class I-based cancer immunosurveillance and immunoevasion. Nat Rev Immunol 21: 116-128, 2021.
28. Mohme M, Riethdorf S and Pantel K: Circulating and disseminated tumour Cells-mechanisms of immune surveillance and escape. Nat Rev Clin Oncol 14: 155-167, 2017.
29. Zou W: Immunosuppressive networks in the tumour environment and their therapeutic relevance. Nat Rev Cancer 5: 263-274, 2005.
30. Wang W, Green M, Choi JE, Gijón M, Kennedy PD, Johnson JK, Liao P, Lang X, Kryczek I, Sell A, *et al*: CD8$^+$ T cells regulate tumour ferroptosis during cancer immunotherapy. Nature 569: 270-274, 2019.
31. Li C, Wang X, Qin R, Zhong Z and Sun C: Identification of a ferroptosis gene set that mediates the prognosis of squamous cell carcinoma of the head and neck. Front Genet 12: 698040, 2021.
32. Lu W, Wu Y, Huang S and Zhang D: A Ferroptosis-related gene signature for predicting the prognosis and drug sensitivity of head and neck squamous cell carcinoma. Front Genet 12: 755486, 2021.
33. Hoadley KA, Yau C, Hinoue T, Wolf DM, Lazar AJ, Drill E, Shen R, Taylor AM, Cherniack AD, Thorsson V, *et al*: Cell-of-Origin patterns dominate the molecular classification of 10,000 tumors from 33 types of cancer. Cell 173: 291-304.e6, 2018.
34. Martens-de Kemp SR BB, Smeets S, Voorham Q, Rustenburg F, de Boer VD, Brink A, van Wieringen WN and Brakenhoff RH: GEO accession number [GSE83519]. NCBI(GEO) (ed.), 2017.
35. Vickers AJ, Cronin AM, Elkin EB and Gonen M: Extensions to decision curve analysis, a novel method for evaluating diagnostic tests, prediction models and molecular markers. BMC Med Inform Decis Mak 8: 53, 2008.
36. Newman AM, Liu CL, Green MR, Gentles AJ, Feng W, Xu Y, Hoang CD, Diehn M and Alizadeh AA: Robust enumeration of cell subsets from tissue expression profiles. Nat Methods 12: 453-457, 2015.
37. Maeser D, Gruener RF and Huang RS: oncoPredict: An R package for predicting in vivo or cancer patient drug response and biomarkers from cell line screening data. Brief Bioinform 22: bbab260, 2021.
38. Livak KJ and Schmittgen TD: Analysis of relative gene expression data using real-time quantitative PCR and the 2(-Delta Delta C(T)) method. Methods 25: 402-408, 2001.
39. Chen XJ, Guo CH, Yang Y, Wang ZC, Liang YY, Cai YQ, Cui XF, Fan LS and Wang W: HPV16 integration regulates ferroptosis resistance via the c-Myc/miR-142-5p/HOXA5/SLC7A11 axis during cervical carcinogenesis. Cell Biosci 14: 129, 2024.
40. Yang J and Gu Z: Ferroptosis in head and neck squamous cell carcinoma: From pathogenesis to treatment. Front Pharmacol 15: 1283465, 2024.
41. Hamid S, Khan MS, Khan MA, Muhammad N, Singh M, Al-Shabeeb Akil AS, Bhat AA and Macha MA: Human papilloma virus infection drives unique metabolic and immune profiles in head and neck and cervical cancers: Implications for targeted therapies and prognostic markers. Discov Oncol 16: 676, 2025.
42. Shen P, Zhang TY and Wang SY: TRIB3 promotes oral squamous cell carcinoma cell proliferation by activating the AKT signaling pathway. Exp Ther Med 21: 313, 2021.
43. Wennemers M, Bussink J, Scheijen B, Nagtegaal ID, van Laarhoven HW, Raleigh JA, Varia MA, Heuvel JJ, Rouschop KM, Sweep FC and Span PN: Tribbles homolog 3 denotes a poor prognosis in breast cancer and is involved in hypoxia response. Breast Cancer Res 13: R82, 2011.
44. Zhou H, Luo Y, Chen JH, Hu J, Luo YZ, Wang W, Zeng Y and Xiao L: Knockdown of TRB3 induces apoptosis in human lung adenocarcinoma cells through regulation of Notch 1 expression. Mol Med Rep 8: 47-52, 2013.
45. Hong B, Zhou J, Ma K, Zhang J, Xie H, Zhang K, Li L, Cai L, Zhang N, Zhang Z and Gong K: TRIB3 promotes the proliferation and invasion of renal cell carcinoma cells via activating MAPK signaling pathway. Int J Biol Sci 15: 587-597, 2019.
46. Miyoshi N, Ishii H, Mimori K, Takatsuno Y, Kim H, Hirose H, Sekimoto M, Doki Y and Mori M: Abnormal expression of TRIB3 in colorectal cancer: A novel marker for prognosis. Br J Cancer 101: 1664-1670, 2009.
47. Tang Z, Chen H, Zhong D, Wei W, Liu L, Duan Q, Han B and Li G: TRIB3 facilitates glioblastoma progression via restraining autophagy. Aging (Albany NY) 12: 25020-25034, 2020.
48. Izrailit J, Jaiswal A, Zheng W, Moran MF and Reedijk M: Cellular stress induces TRB3/USP9x-dependent Notch activation in cancer. Oncogene 36: 1048-1057, 2017.
49. Hua F, Mu R, Liu J, Xue J, Wang Z, Lin H, Yang H, Chen X and Hu Z: TRB3 interacts with SMAD3 promoting tumor cell migration and invasion. J Cell Sci 124: 3235-3246, 2011.
50. Zhang XD, Liu ZY, Wang MS, Guo YX, Wang XK, Luo K, Huang S and Li RF: Mechanisms and regulations of ferroptosis. Front Immunol 14: 1269451, 2023.
51. Zhu X, Zhang F, Zhang W, He J, Zhao Y and Chen X: Prognostic role of epidermal growth factor receptor in head and neck cancer: A meta-analysis. J Surg Oncol 108: 387-397, 2013.
52. Lv D, Zhong C, Dixit D, Yang K, Wu Q, Godugu B, Prager BC, Zhao G, Wang X and Xie Q: EGFR promotes ALKBH5 nuclear retention to attenuate N6-methyladenosine and protect against ferroptosis in glioblastoma. Mol Cell 83: 4334-4351.e7, 2023.
53. Zhang Q, Li N, Deng L, Jiang X, Zhang Y, Lee LTO and Zhang H: ACSL1-induced ferroptosis and platinum resistance in ovarian cancer by increasing FSP1 N-myristylation and stability. Cell Death Discov 9: 83, 2023.
54. Qin Y, Pei Z, Feng Z, Lin P, Wang S, Li Y, Huo F, Wang Q, Wang Z, Chen ZN, *et al*: Oncogenic activation of YAP signaling sensitizes ferroptosis of hepatocellular carcinoma via ALOXE3-mediated lipid peroxidation accumulation. Front Cell Dev Biol 9: 751593, 2021.
55. Han L, Bai L, Qu C, Dai E, Liu J, Kang R, Zhou D, Tang D and Zhao Y: PPARG-mediated ferroptosis in dendritic cells limits antitumor immunity. Biochem Biophys Res Commun 576: 33-39, 2021.
56. Sabatier M, Birsen R, Lauture L, Mouche S, Angelino P, Dehairs J, Goupille L, Boussaid I, Heiblig M, Boet E, *et al*: C/EBPα confers dependence to fatty acid anabolic pathways and vulnerability to lipid oxidative Stress-induced ferroptosis in FLT3-Mutant leukemia. Cancer Discov 13: 1720-1747, 2023.
57. Cui Z, Fu Y, Yang Z, Gao Z, Feng H, Zhou M, Zhang L and Chen C: Comprehensive analysis of a ferroptosis pattern and associated prognostic signature in acute myeloid leukemia. Front Pharmacol 13: 866325, 2022.
58. Meng J, Du H, Lu J and Wang H: Construction and validation of a predictive nomogram for ferroptosis-related genes in osteosarcoma. J Cancer Res Clin Oncol 149: 14227-14239, 2023.
59. Zhang J, Deng Y, Zhang H, Zhang Z, Jin X, Xuan Y, Zhang Z and Ma X: Single-cell RNA-Seq analysis reveals ferroptosis in the tumor microenvironment of clear cell renal cell carcinoma. Int J Mol Sci 24: 9092, 2023.
60. Jiang W, Song Y, Zhong Z, Gao J and Meng X: Ferroptosis-related long Non-Coding RNA signature contributes to the prediction of prognosis outcomes in head and neck squamous cell carcinomas. Front Genet 12: 785839, 2021.
61. Friedmann Angeli JP, Krysko DV and Conrad M: Ferroptosis at the crossroads of Cancer-acquired drug resistance and immune evasion. Nat Rev Cancer 19: 405-414, 2019.